batteries

MDPI

Article

Stress and Strain Characterization for Evaluating Mechanical Safety of Lithium-Ion Pouch Batteries under Static and Dynamic Loadings

Edris Akbari and George Z. Voyiadjis *

Department of Civil and Environmental Engineering, Louisiana State University, Baton Rouge, LA 70803, USA
* Correspondence: voyiadjis@eng.lsu.edu

Abstract: The crashworthiness of electric vehicles depends on the response of lithium-ion cells to significant deformation and high strain rates. This study thoroughly explores the mechanical behavior due to damage of lithium-ion battery (LIB) cells, focusing on Lithium Nickel Manganese Cobalt Oxide (NMC) and Lithium Iron Phosphate (LFP) types during both quasi-static indentation and dynamic high-velocity penetration tests. Employing a novel approach, a hemispherical indenter addresses gaps in stress–strain data for pouch cells, considering crucial factors like strain rate/load rate and battery cell type. In the finite element method (FEM) analysis, the mechanical response is investigated in two stages. First, a viscoplastic model is developed in Abaqus/Standard to predict the indentation test. Subsequently, a thermomechanical model is formulated to predict the high-speed-impact penetration test. Considering the high plastic strain rate of the LIB cell, adiabatic heating effects are incorporated into this model, eliminating heat conduction between elements. Addressing a notable discrepancy from prior research, this work explores the substantial reduction in force observed when transitioning from a single cell to a stack of two cells. The study aims to unveil the underlying reasons and provide insights into the mechanical behavior of stacked cells.

Keywords: lithium-ion batteries; mechanical safety; indentation; impact; crashworthiness; electric vehicle

Citation: Akbari, E.; Voyiadjis, G.Z. Stress and Strain Characterization for Evaluating Mechanical Safety of Lithium-Ion Pouch Batteries under Static and Dynamic Loadings. *Batteries* **2024**, *10*, 309. https://doi.org/10.3390/batteries10090309

Academic Editor: Zhenbo Wang

Received: 25 July 2024
Revised: 25 August 2024
Accepted: 29 August 2024
Published: 31 August 2024

1. Introduction

Due to their high energy density, lithium-ion batteries (LIBs) are primary energy storage systems for electric vehicles and defense markets [1]. LIBs might be exposed to various loading conditions during crush cases. Although structural components and specially designed shields protect LIBs in electric vehicles to avoid mechanical damage to battery cells caused by a crush [1], significant fires in electric cars are still being reported. Therefore, the safety issue of commercial LIBs under high-velocity penetration (crush case) requires further investigation.

The investigation of the penetration tests can be categorized into three categories based on the projectile impact velocity [2]. The first classification relates to low-velocity penetration (less than 50 m/s), in which thin plates are typically penetrated by a drop-weight structure [3,4]. In the second, projectiles are accelerated by a compressed air gas gun to penetrate plates at velocities between 50 and 1300 m/s [5]. The third is hypervelocity impact (more than 1300 m/s) [6,7]. However, it should be noted that various projectile velocities in the penetration test result in different strain rates ($\dot{\varepsilon}$) regimes [8], such as:

- Static, $\dot{\varepsilon} < 10^{-4}\ s^{-1}$;
- Quasi-static, $10^{-4} < \dot{\varepsilon} < 10^{-2}\ s^{-1}$;
- Intermediate rate, $10^{-2} < \dot{\varepsilon} < 10\ s^{-1}$;
- Dynamic, $10 < \dot{\varepsilon} < 10^{3}\ s^{-1}$;
- Shock, $\dot{\varepsilon} > 10^{3}\ s^{-1}$.

In recent years, the majority of studies have been performed on the mechanically induced internal short circuit (ISC), including mechanical abuse experiments with different loading directions (out-of-plane compression [9], pinch [10], indentation [11–16], nail penetration [15,17–19], three-point bending [11,14], etc.). Nonetheless, the state of charge (SOC) of the cell [20], loading direction [17,21], and load rate [1] play significant roles in the mechanical behavior of LIB cells under different loading scenarios. Chung et al. [17] subjected a large format pouch cell to local indentation with three different indenter shapes: flat cylindrical (44.5 mm), hemispherical punch with radii (12.6 mm, 28.6 mm, 44.5 mm, and 90 mm), and conical punch with radii (15 mm, and 28.6 mm) and concluded that the slant fracture is invariant concerning all indenter diameters, sizes, and orientation. In addition to all the mechanical factors, electrical aging significantly affects LIB cells' mechanical properties [22]. However, considering all critical factors in one study and developing a finite element model (FEM) to predict their behavior remains a significant challenge. In this study, two major factors were investi-gated, strain rate or load rate (from quasi-static to dynamic loading rate), and type of battery cell (Lithium Nickel Manganese Cobalt Oxide, and Lithium Iron Phosphate).

In pioneer investigations of mechanical abuse in the LIB cell, most experiments were conducted under quasi-static conditions. Compared to studies on deformation at quasi-static loading rates, there are few reports on LIB cell evaluations in high-velocity penetration tests [23]. Kisters et al. [4] conducted the penetration test by a hemispherical punch with a diameter of 12.7 mm with velocities between 0.01 mm/s and 5000 mm/s for the elliptical and pouch cells. According to their results, the critical force value increased as the load rate increased for elliptical cells but decreased for pouch cells. Fras et al. [1] performed a high-velocity projectile penetration test with pouch cells at the penetration velocity of 360,000 mm/s. However, following the literature review, the question must be posed as how the optimal constitutive equation can predict the LIB cell's mechanical response at varied loading rates. Addressing this discrepancy constitutes a primary objective of this paper, aimed at elucidating the underlying reasons for this observed phenomenon. The study conducted quasi-static indentation tests to find an appropriate constitutive equation. This equation was then adapted for high-impact tests, establishing a bridge between quasi-static and dynamic situations.

Nevertheless, load (P) and displacement (h) are continuously recorded during the indentation test. It is essential to have stress—strain data, which is beneficial for the analysis, design, and prediction of the mechanical behaviour behavior of the LIB cell under indentation tests. In the authors' previous research, cylindrical cells were indented with a cylindrical indenter, and a novel formulation was created to convert force—displacement data into stress—strain data [24,25]. The primary objective of this investigation is to address a gap within existing experimental tests. This involves characterizing stress—strain data obtained from applying a hemispherical indenter on the pouch cell and formulating a damage criterion at the cell level. Consistency across varying loading conditions is en-sured by employing the same projectile geometry in both tests and extracting the constitutive equation from the static loading.

Wang et al. [26] investigated pouch cells utilizing a spherical indenter with a diameter of 12.7 mm, examining both single cells and stacks of three cells. In the case of a single cell, the maximum force applied was noted as 14 kN, resulting in a displacement of 5 mm. However, for the three-cell stacks, the maximum force experienced a significant reduction to 4 kN with a corresponding displacement of 4 mm. Notably, the study did not provide an explicit rationale for this substantial decrease in force when transitioning from a single cell to a stack of three cells. Addressing this discrepancy constitutes a primary objective of this paper, aimed at elucidating the underlying reasons for this observed phenomenon.

In contrast to prior experimental approaches [27], this study probes an important distinction in the experimental setup concerning pouch cells, characterized by thinner profiles compared to prismatic cells. Specifically, the phenomenon of bulging effects occurring beyond a certain penetration depth during indentation tests on pouch cells is highlighted.

This effect generates a reaction force from the base, necessitating consideration of force-displacement results. To address this challenge, a homemade fixture was developed and strategically designed to maintain space between the sample and the base grip, effectively mitigating the influence of the reaction force from the base grip. Furthermore, the approach diverges in the failure model employed [27]. While previous models [27] typically consider mechanical factors alone, this study endeavors to couple thermal and mechanical aspects, acknowledging the influence of friction between the projectile and sample. However, given the rapid deformation inherent in high-speed impact tests, conventional methods of thermal dissipation are quite impractical. To circumvent this limitation, an adiabatic methodology is adopted to account for the instantaneous nature of heat dissipation during impact events.

In prior studies [1,27,28], the Johnson—Cook (JC) material model has been utilized to formulate damage models. In this investigation, a novel approach was undertaken. Initially, quasi-static indenta-tion tests were conducted, and an analytical model was developed to convert force—displacement data into stress—strain information. Subsequently, this analytical model was validated against finite element (FE) simulations. Moving forward, high-speed penetration tests were performed. Notably, this methodology diverges from conven-tional practices found in the literature, where material parameters are typically ex-perimentally obtained through tensile or compression tests or by an inverse method for FE model development aimed at predicting the behavior of lithium-ion bat-teries under high-impact scenarios. Instead, the same geometry was employed for both static and dynamic testing. Consequently, the stress—strain data derived from the in-dentation tests were leveraged for the high-impact tests, establishing a robust correla-tion between low-speed and high-speed scenarios, thereby enhancing the precision of simulation outcomes. Moreover, an inverse technique was employed to determine the material properties of the damage model.

2. Materials and Methods

2.1. Materials

In this investigation, two different types of pouch cells were evaluated. The first is Lithium Nickel Manganese Cobalt Oxide (NMC) with 72% SOC, and the second is Lithium Iron Phosphate (LFP) with 72% SOC, as shown in Figure 1b,c. Table 1 provides the specifications for each cell type.

Table 1. Specifications of pouch LFP and NMC battery cells.

Item	Specification NMC	Specification LFP
Size	142 × 190 × 8.3 mm^3	163 × 163 × 9.7 mm^3
Nominal capacity	8 Ah	25 Ah
Standard charge current	1 C	0.2 C
Weight	204 g	505 g
Nominal voltage	3.7 V	3.2 V
Charge cut-off voltage	4.2 V	3.65 V
Discharge cut-off voltage	2.75 V	2 V

Given the complex composition of lithium-ion battery (LIB) cells, which consist of various components, including the anode, cathode, and separator, the conventional approach of extracting dogbone samples for tensile testing becomes unfeasible. Therefore, an innovative approach was proposed by utilizing indentation tests as a practical alternative to obtain stress—strain data. The indentation test provides a valuable method for determining stress—strain curves in situations where traditional tensile testing is impractical or impossible, as is often the case with LIB cells.

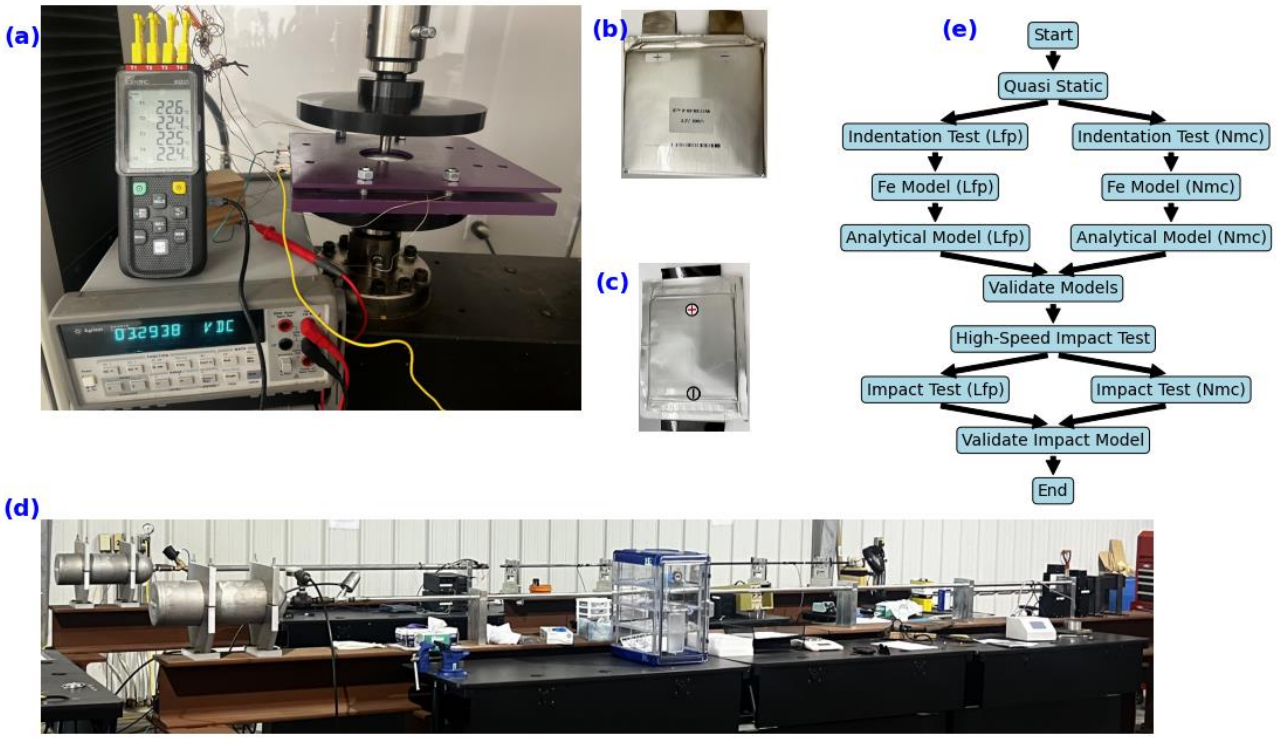

Figure 1. (**a**) Experimental setup for the indentation test. (**b**) LFP pouch cell. (**c**) NMC pouch cell. (**d**) The impact penetration test. (**e**) Flow chart: the experimental setup includes an indentation test for both LFP and NMC pouch cells, as well as a high-speed impact penetration test to validate the models.

2.2. Quasistatic Condition (Indentation Test)

The Electromechanical MTS Insight performs an indentation test at three different loading speeds (0.02, 2, and 4 mm/s), which were set to evaluate the strain rate effect on LIB cells' mechanical behavior.

Since pouch cells have a layered structure, their mechanical response to the indentation test differs from that of bulk material. As one of the approaches of this research, an in-house-made fixture was designed to prevent wrinkling in the pouch cell during the indentation test (as shown in Figure 1a). In contrast to previous research [11–15], this novel fixture design ensures that force-displacement data originate from the battery cell, not the MTS machine's bottom platen.

2.3. Dynamic Condition (High-Velocity Penetration Test)

This investigation included the performance of high-velocity penetration experiments on pouch cells using a gas gun, as seen in Figure 1d. The gas gun is used to propel a projectile through its enclosed tube to conduct impact penetration tests on the pouch cells. The projectile's mass is 30.42 g, and the length and radius are 34 mm and 6 mm, respectively.

The gas gun used in this study is equipped with two laser sensors specifically designed for the measurement of the initial velocity of the projectile, referred to as V_0. In addition, the experimental setup includes the integration of second laser barriers to accurately measure the residual velocities, denoted as V_r.

2.4. Voltage

The in-situ voltage of LIB cells was measured during indentation and high-velocity penetration tests by using an Agilent 34410A Digital Multimeter (Keysight, Santa Rosa, CA, USA) with an accuracy of 0.0001 mV. The assessment of voltage is most significant in identifying the existence of internal short circuits inside the cells. The occurrence of an

internal short circuit results in a rapid decrease in voltage, which is a critical observation for detecting any problems or irregularities inside the battery cells.

2.5. Temperature

In the conducted experimental study, a high-precision thermometer with four thermocouple probes was used to precisely assess temperatures throughout a broad spectrum. The thermometer has the following specifications: it is precisely engineered to accurately detect temperatures between −200 °C and 1372 °C, rendering it appropriate for various applications. The thermometer has remarkable precision, with a variance of just ±0.1% of the measured value.

Figure 1e illustrates the experimental setup for high-speed impact penetration tests conducted to validate computational and analytical models. These tests involve subjecting both LFP and NMC pouch cells to rapid impact forces in order to simulate real-world scenarios such as collisions or punctures. The flowchart outlines the sequence of steps involved in the experimental validation process, including the quasi-static indentation tests, finite element modelling of cell behavior, and comparison with analytical predictions. By visually depicting the experimental setup and validation procedure, Figure 1e provides a comprehensive overview of the methodology employed to assess the performance and behavior of the battery cells under extreme conditions.

3. Results

3.1. Indentation Test

3.1.1. Experimental Results

In previous studies [4,14,26,29–35], indentation tests on pouch cells were often conducted without considering the influence of the mechanical machine's platen. This approach resulted in an oversight, as the indentation caused a bulge in the pouch cell beyond a critical depth, leading to a rapid increase in force values.

To evaluate this effect, in this research, three scenarios were employed for indentation tests, as depicted in Figure 2: the first scenario without a fixture, represented as 'hard base'; the second scenario with one sample positioned between the fixture, denoted as 'one sample'; and the third scenario involved stacking two samples in the fixture, represented as 'two samples'. Indentation tests were conducted under three different load rates for the latter scenario.

In this study, when varying the base, the load rate was kept constant at 0.02 mm/s to isolate the effect of the base change on the material response. This approach allowed for a clear understanding of how the base influences the mechanical behavior of the cells. Conversely, when varying the load rate, the base remained constant, and two samples were tested in the fixture. This setup ensured that any observed differences in mechanical response could be attributed solely to changes in the load rate. These methodological choices were made to provide precise and reliable data, and this will be clarified in the manuscript to avoid any potential confusion.

In the initial phase of the investigation, the objective is to elucidate the impact of the base conditions and design a custom fixture to mitigate this effect. The experimental setup involved placing the sample between the bottom platen (referred to as the base in this study) and the indenter (connected to the upper platen) before conducting the test. Analyzing the force versus penetration depth data for pouch cells under base conditions for NMC and LFP types, as shown in Figure 2, revealed a substantial increase in force values with increasing penetration depth. The results indicated a maximum force of 6.3 kN for NMC samples, while LFP samples exhibited a slightly different pattern, peaking at around 7.8 kN. These findings underscore the significant influence of the base conditions on force-displacement behavior, demonstrating the necessity of considering this factor in the indentation tests.

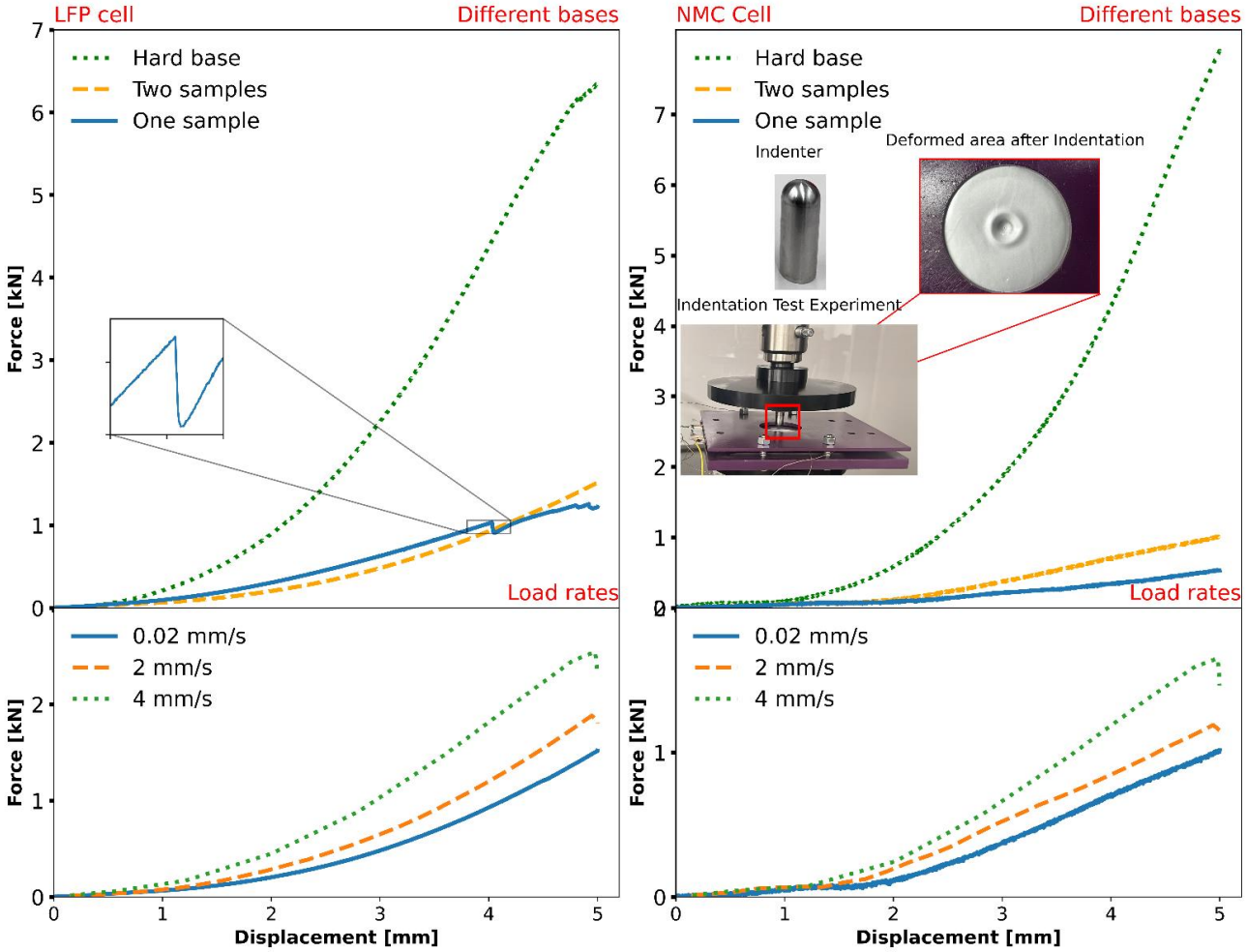

Figure 2. Force-displacement curve on LIB cells under the Indentation tests in different rates and boundary conditions.

Indentation tests were conducted using a homemade fixture to mitigate the influence of the base and bulging effects, introducing an innovative approach to capture force-displacement data during indentation tests without being affected by reaction forces from the bottom platens. This methodology deviates from conventional practices outlined in the existing literature [26,29,36]. In the second scenario, a pouch cell sample (NMC or LFP) was positioned in the fixture, consisting of two rectangular plates with a hole for applying load to the cell via an indenter. During testing, the indenter initially tended to push into the cell through the hole rather than penetrating inside. Subsequently, the presence of sharp edges around the hole induced an initial fracture, resulting in an amplified peak and subsequent drop in the force-displacement data. These observations underscore the intricate nature of the indentation process and highlight the necessity of thoughtful fixture design to capture material response accurately during the indentation tests.

Additionally, wrinkling was observed post-penetration, possibly influenced by the sharp edges of the hole. This phenomenon suggests that the edge of the hole in the fixture could contribute to post-indentation effects, leading to observable changes in the cell structure. These findings contribute to a more comprehensive understanding of the intricacies involved in indentation testing, emphasizing the importance of fixture design considerations for reliable and accurate material characterization.

In the third scenario, a stack of two pouch cell samples (NMC and LFP) was tested in the fixture to conduct indentation tests. When comparing with the first scenario, the results reveal that the maximum load in the first scenario is around five and six times higher than in the third scenario for LFP and NMC indentations, respectively, as depicted in Figure 2.

This substantial difference underscores the significant impact of the base platen on the force-displacement results. Moreover, in comparison with the second scenario, no drop in force was observed, indicating the successful elimination of the sharp edge effect from the fixture on the force-displacement data. With these corrections, it can be confidently claimed that all force-displacement data originating from NMC and LFP samples in the third scenario are trustworthy.

The third scenario setup aimed to eliminate the influence of the base platen, fixture's structure, and the hole's edges. The results from this configuration provide compelling evidence that, in indentation tests, it is crucial to limit the penetration depth to below 20% of the total thickness. Beyond this threshold, the effect of the bottom platen becomes significant, influencing and controlling the final reaction force in the indentation test, rather than solely reflecting the behaviour of the LIB cells.

It is worth noting that this configuration significantly enhances the reliability of data obtained from the indentation test. The force-displacement curves reveal an initial linear stage succeeded by a force plateau, occurring approximately at 1 mm and 2 mm for LFP and NMC indentations, respectively. No instances of short circuits are identified under the static loading rate condition (0.02 mm/s), with the force showing a slight decrease after a displacement of 5 mm. However, deeper penetrations beyond 5 mm are necessary to explore potential internal short circuits

The results in Figure 2 reveal a notable discrepancy in peak force values, with LFP samples registering around 2 kN, while NMC samples exhibit approximately 1 kN. This observed difference suggests that strain hardening in the LFP samples is more pronounced than in the NMC samples.

After establishing and confirming the impact of the bottom platen, the focus shifts to evaluating the influence of the load rate, which inherently represents the effect of the strain rate. Given the ultimate goal of developing a constitutive equation applicable to high-speed penetration tests, three different strain rates (0.002, 2, and 4 mm/s) were selected for both LFP and NMC samples.

The obtained results indicate a clear correlation between the load rate and the peak force values. As illustrated in Figure 2, an increase in the load rate corresponds to an elevation in the peak force. Notably, the data highlights that the increase in peak force with an escalating load rate is more pronounced in LFP cells compared to NMC cells. This observation underscores the significance of considering and understanding the strain rate effect, providing valuable insights for the development of a robust constitutive equation tailored for high-speed penetration tests.

3.1.2. Computational Model

For the simulation of the indentation test, ABAQUS/Standard was employed to develop finite element models for the indentation. The indenter was modelled as a rigid body using 1457 linear quadrilateral elements of type R3D4, with its motion controlled by the rigid body reference node. At the reference node, displacement control was also designated for the indenter, ensuring consistent physical characteristics in quasi-static conditions.

Since the hemispherical-shaped indenter was expected to induce circular deformations in the LIB cells after indentation or penetration, a refined mesh was employed, as depicted in Figure 3a, to create a circular region in the center of the LIB samples. This refined mesh not only served to reduce computational time by utilizing finer mesh elements in the center and coarser mesh elements in areas far from the center where no deformation occurred but also ensured the best contact area and stress distribution, closely mirroring the results of experimental tests. It is important to mention that 84,000 linear hexahedral elements of the C3D8R type were used for the LIB cell.

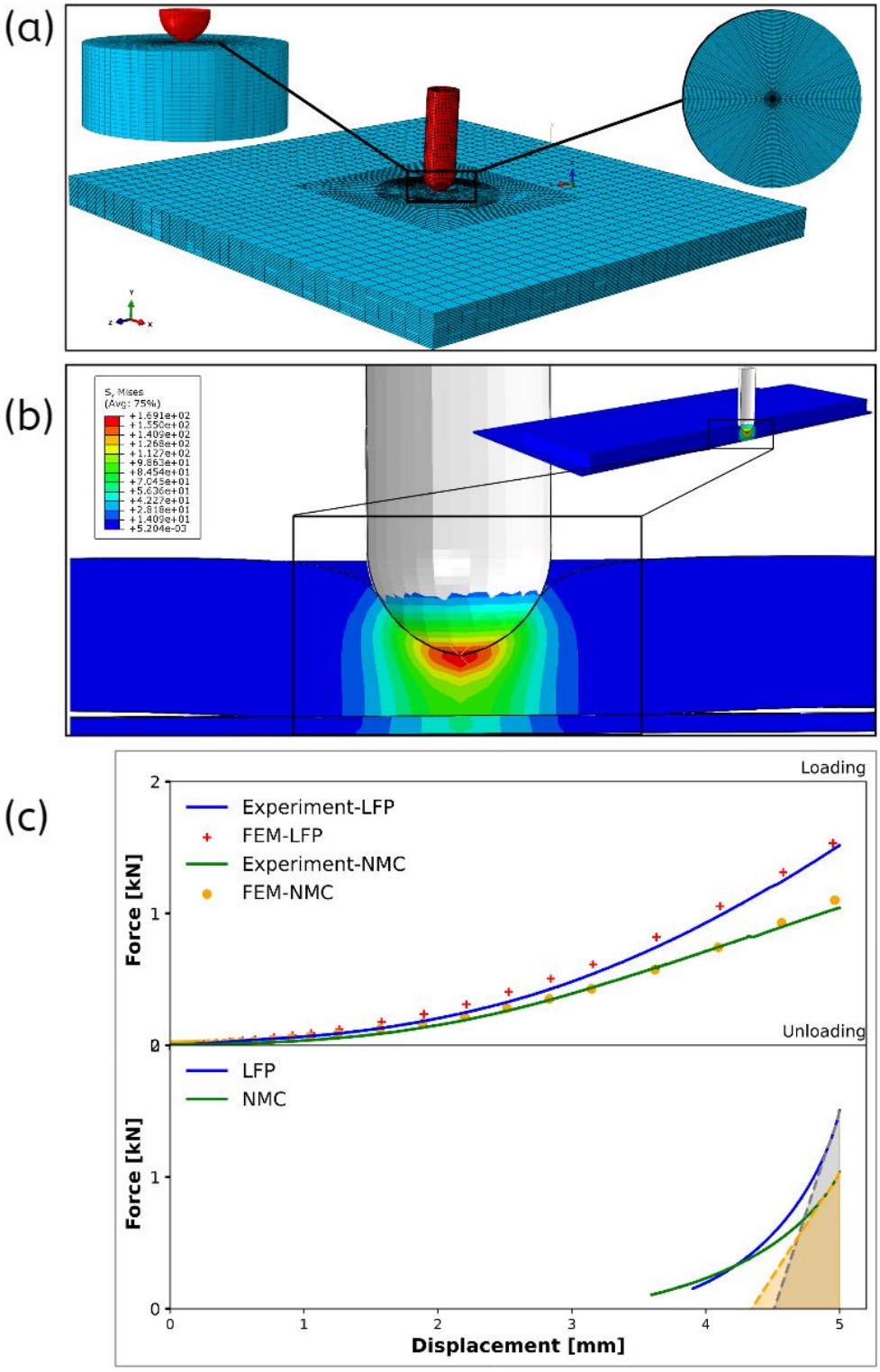

Figure 3. (**a**) Force–displacement in single-loading during the Iindentation test and analysis of unloading segment slopes for Young's modulus determination. (**b**) Simulation cross-section: impact of me-chanical base conditions on pouch cell indentation. (**c**) Force–displacement in single-loading during Tthe Iindentation test and analysis of unloading segment slopes for Young's modulus determination.

Before investigating the specifics of the computational model, it is crucial to further validate the observations from the initial experimental scenario. To achieve this, a Finite

Element Method (FEM) model of the pouch cell on the steel platen was constructed, as shown in Figure 3b. This model offers a sectional view, illustrating the stress distribution within the lithium-ion battery (LIB) cell and the base. Notably, the indentation force caused the cell to bend, acquire a concave shape, and separate from the steel platen underneath, aligning with the experimental findings. The simulation affirmed the existence of a bulge in the LIB cell, exerting a notable impact on reaction force values. This additional validation enhances the reliability of the computational model and reinforces the consistency between simulated and experimental outcomes.

Comparing these computational results with the experimental findings, especially in the third scenario involving a stack of two pouch cell samples (NMC and LFP) in the fixture, highlighted the substantial difference in the maximum load between the first and third scenarios. To ensure a comprehensive analysis in this research, the third scenario from the previous experimental section was selected to evaluate the LIB cell's behavior under indentation testing conditions in the computational model.

Developing viscoplastic constitutive models for LIB cells is essential to support the design of secure vehicles through finite element simulations. The behavior of the homogenized LIB cells is modelled using a viscoplastic formulation that incorporates strain hardening and strain rate sensitivity, as follows [37,38]:

$$\sigma = \left(A + B\varepsilon_p^n\right)\left(1 + C\ln\left(\frac{\dot{\varepsilon}_p}{\dot{\varepsilon}_0}\right)\right) \quad (1)$$

where σ is the equivalent stress, ε_p is the equivalent plastic strain, and $\dot{\varepsilon}_p$ is the equivalent plastic strain rate. In addition, A, B, n, and C are the four material parameters in the model that characterize the yield stress (A), the strain hardening (B and n), and the strain rate sensitivity (C), respectively.

As previously discussed in the preceding section, other factors may be considered in Equation (1), including temperature, the size of the indenter, and the effect of SOC. The complexity of the constitutive equation is temporarily set aside, directing attention towards a primary inquiry that must be addressed to derive stress-strain curves from indentation data. The characterization of material parameters is a subject of ongoing research.

Clyne et al. [39] conducted an investigation to evaluate the indentation profile, which represents the desired result for the profilometry-based inverse finite element method (FEM) used in the modelling of the experiment. The objective is to identify the most favorable combination of parameter values within a constitutive rate-dependent plasticity law, with a special focus on the true stress–true strain connection. Nevertheless, this methodology necessitates using specialist equipment for profile assessment, resulting in escalated expenses associated with conducting the tests, such as Stylus [40] and Optical Metrology [41].

Another methodology that may be used is the inverse finite element method (FEM) based on force-displacement. The loading segment of the predicted force-displacement graph is compared with empirical test data to determine plasticity parameters, including A, B, and n, and indicate the value for the contact area. Concurrently, the unloading segment of the experimental test data is used to ascertain the elastic stiffness [21,24,42,43]. Hence, the optimization model was employed in this research endeavor in the following manner:

$$\text{minimize} : F(x) = \sum_{i=1}^{N} \frac{\left(P(x)_i^{pre} - P_i^{exp}\right)^2}{2} \quad (2)$$

The objective function, denoted as F, represents the goal of a multi-variable optimization problem. In this context, the variable x corresponds to the elastoplastic material parameters A, B, C, and n as defined in Equation (1). Variables $P(x)_i^{pre}$ and P_i^{exp} represent the anticipated and experimental forces obtained from the indentation test, respectively.

This study performed an indentation test on both pouch battery cells to ascertain Young's modulus, resulting in values of 0.39 GPa for LFP and 0.31 GPa for NMC, as illustrated in Figure 3c. The emphasis is on the slopes of the unloading segments, crucial for determining Young's modulus, providing valuable insights into the material's elastic behavior under indentation conditions. The subsequent objective was identifying additional material parameters in Equation (1), corresponding to the plastic region. Consequently, an optimization model was deployed to enhance the estimates of the elastoplastic material parameters A, B, C, and n. This model evaluated the loading segment of the predicted force-displacement graph, aligning it with empirical test data to determine plasticity parameters.

Tables 2 and 3 outline the results of the minimization method for NMC and LFP samples, offering critical insights into optimized material properties derived from the indentation test results of LIB cells. In doing so, the experimental data for measuring Young's modulus and the computational model are intricately integrated, forming a robust constitutive equation that predicts the pouch cell's behavior under indentation.

Table 2. Material parameters for minimization: values used for LFP cells.

	Initial Value	Lower Values	Upper Values	Target Values
A (MPa)	1	0.01	10	8
B (MPa)	200	10	2100	1800
n	1.8	0.8	2.3	1.7
c	0.5	0.01	1.5	1.25

Table 3. Material parameters for minimization: values used for NMC cells.

	Initial Value	Lower Values	Upper Values	Target Values
A (MPa)	1.2	0.01	8	0.08
B (MPa)	110	8	1800	60
n	1.4	0.7	1.7	1.82
c	0.3	0.01	1.25	0.27

3.1.3. Analytical Model

In the pursuit of developing a comprehensive understanding, this study employed the same cylindrical indenter with a spherical head for both high-impact penetration and indentation tests. Figure 4 offers a schematic illustration, elucidating key parameters such as contact radius, indentation depth, load, and indenter radius. The selection of this indenter configuration is supported by its efficiency in facilitating deep penetration tests, ensuring sufficient deformation zones across a broad spectrum of plastic strains [43–45]. This approach uniquely captures the elastoplastic behavior of materials characterized by power-law-like features, while concurrently minimizing the strain gradient effect and reducing the risk of cracking compared to a sharp indenter [46,47].

Having discussed the experimental facets and the development of a finite element model for indentation tests, the focus now shifts towards the analytical modelling aspect. This crucial phase seeks to bridge the existing gap by transforming the indentation load-depth (P-h) curve into an effective stress-strain curve. To accomplish this, an exploration into the formulation of an analytical model is undertaken, establishing a systematic framework for transforming force-displacement data into meaningful stress-strain insights.

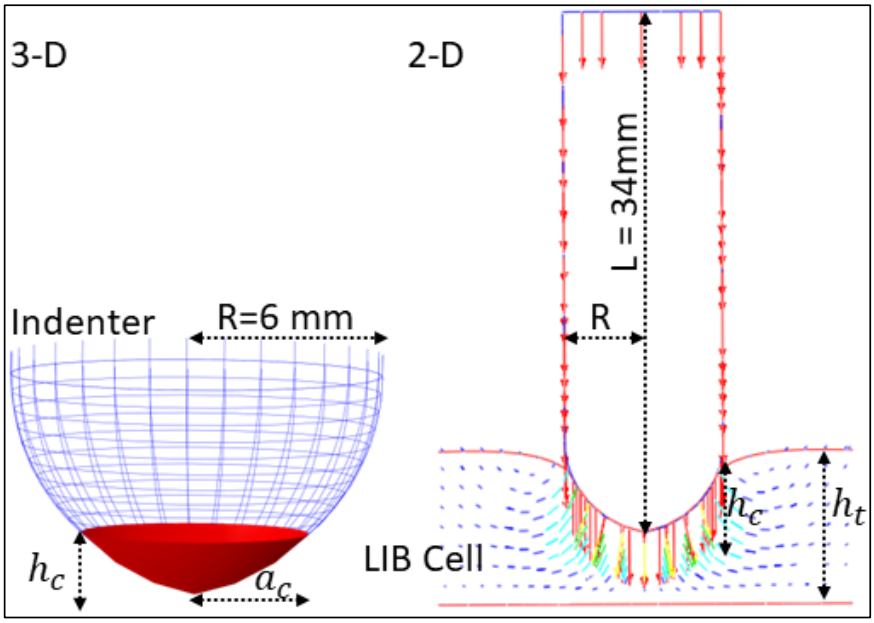

Figure 4. Schematic illustration of indentation: contact radius, indentation depth, load, and indenter radius.

In the analysis of the experimental data obtained from indentation tests, a Gaussian smoothing method was applied to enhance the accuracy and clarity of the force measurements. The Gaussian smoothing technique effectively reduces noise and fluctuations in the force data, providing a more refined representation of the underlying trends. This pre-processing step is crucial for subsequent analyses, especially when converting force-displacement data to effective stress and effective strain. By reducing the noise, the Gaussian smoothing method ensures a more robust and reliable foundation for deriving critical mechanical properties, facilitating a more accurate interpretation of the material's behaviour under compression.

Before embarking on developing an analytical model, it is essential to acknowledge that Hertz's theory [48] postulates frictionless contact between homogeneous elastic bodies with parabolic-shaped surfaces. Nevertheless, the research presented in this study does not include the possible impact of interfacial friction, surface roughness, and pre-existing residual stress, primarily due to the lack of information. Hertz's theory of contact mechanics may be summarized as follows:

$$P = \frac{4}{3} E_{eff} h_e^{\frac{3}{2}} R_{eff}^{\frac{1}{2}} \tag{3}$$

The variables P and h_e represent the indentation load and elastic penetration depth, respectively.

The definitions of the Effective Young's modulus (E_{eff}) [49], and Effective Radius (R_{eff}) are as follows:

$$E_{eff} = \frac{\sqrt{\pi} S}{2\sqrt{A}} \tag{4}$$

where S $\frac{dp}{dh_e}$ refers to the elastic stiffness, essentially the inclination of the unloading curve:

$$R_{eff} = R \tag{5}$$

where R is used to denote the radius of the indenter. Accurately determining the contact area is essential for establishing effective stress based on experimental data.

Therefore, the anticipated contact radius (a_c) is defined as follows.

$$a_c = \sqrt{2 h_c R - h_c^2} \tag{6}$$

where h_c is the contact depth being obtained from elastic and total penetration depth:

$$h_c = 0.667 h_t \tag{7}$$

Therefore, the contact area (A_c) can be used to derive the effective stress:

$$\sigma_{eff} = \frac{P}{\alpha A_c} = \frac{P}{\pi a_c^2} \tag{8}$$

where α is the stress constraint factor.

Due to the impracticality of experimentally measuring contact area during indentation tests, Finite Element Method (FEM) modelling offers a viable alternative for obtaining this crucial information. Equation (8) presents an analytical model for determining contact area based on contact radius (a_c) in this study. The analytical results exhibit a strong agreement with FEM outcome, as shown in Figure 5.

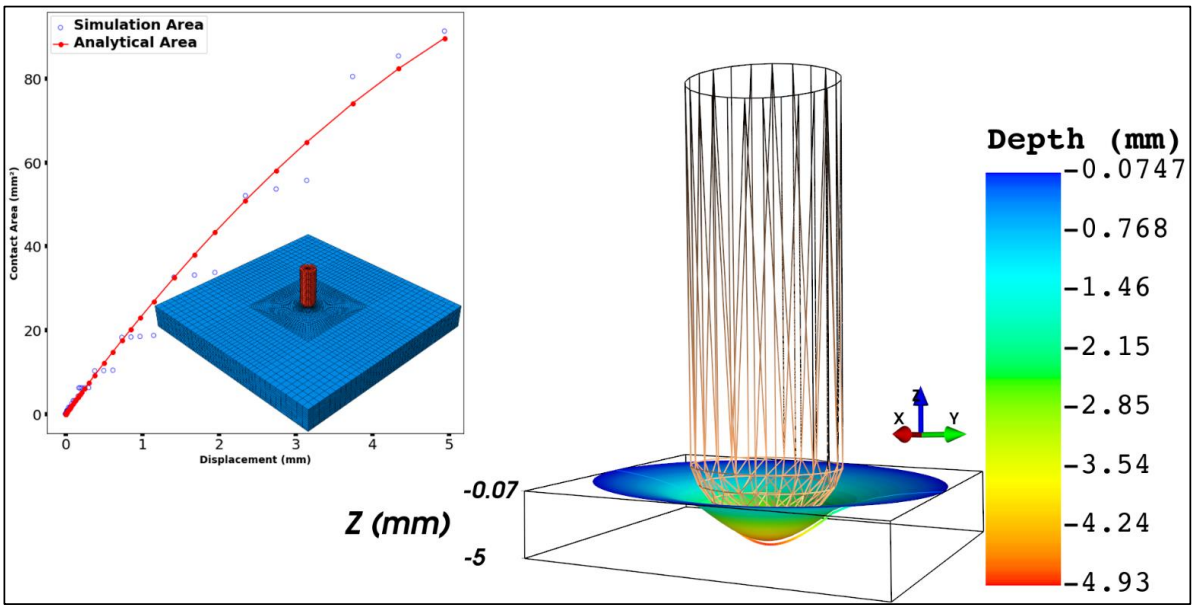

Figure 5. Graphical representation of the contact area between the indenter and top surface of the cell, and the calculated contact area from the analytical and FE model.

In previous publications [24,25], a cylindrical rod was employed over a cylindrical battery cell in an indentation test, and the effective strain was calculated using specific formulae. However, these conventional formulations provide a physically meaningful interpretation of indentation strain when plastic deformation extends deeper and spreads radially within the LIB cell during testing. While recognizing the challenges associated with calculating contact area, the same definition was used for indentation strain in this current work, utilizing a hemispherical indenter on a pouch cell. The newly proposed strain components, denoted as ε_{xx}, ε_{yy}, and ε_{zz}, are related to the contact dimensions a, b, and h_c, respectively. The effective indentation strain, ε_{eff}, is then calculated as a composite measure using these components, providing a comprehensive representation of the indentation-induced deformation in the pouch cell. This novel approach aims to address the limitations observed in previous studies and enhance the accuracy of strain characterization in indentation tests:

$$\varepsilon_{xx} = \varepsilon_{yy} = \frac{a_c}{R} \tag{9}$$

$$\varepsilon_{zz} = \frac{h_c}{R} \tag{10}$$

Hence, the calculation of the effective indentation strain is as follows:

$$\varepsilon_{\text{eff}} = \frac{1}{\beta}\sqrt{\frac{3}{2}\left(\varepsilon_{xx}^2 + 2\varepsilon_{xx}^2\right)} \tag{11}$$

where β is the strain constraint factor.

Subsequently, by comparing Equations (8) and (11) from the analytical section with the FEM model, the two parameters (α and β) in the analytical model can be ascertained. The values are determined to be $\alpha = 0.62$ and $\beta = 8$. Moreover, the contours of effective stress beneath the indenter, depicted in Figure 6, showcase the influence of the spherical shape of the indenter in the finite element model, validated against experimental data for the pouch cell indentation test. It is noteworthy that at the initial stages of the indentation test, insufficient contact between the indenter and the top surface, along with existing gaps between different layers within the pouch battery cell, may influence the accuracy of stress-strain data. As the indentation progresses, the layers gradually consolidate, leading to an increase in load and a more reliable measurement of stress-strain behavior. This comprehensive procedure seamlessly integrates analytical, experimental, and simulation models, with each component validating the others. Consequently, the final dataset derived from this approach is deemed trustworthy.

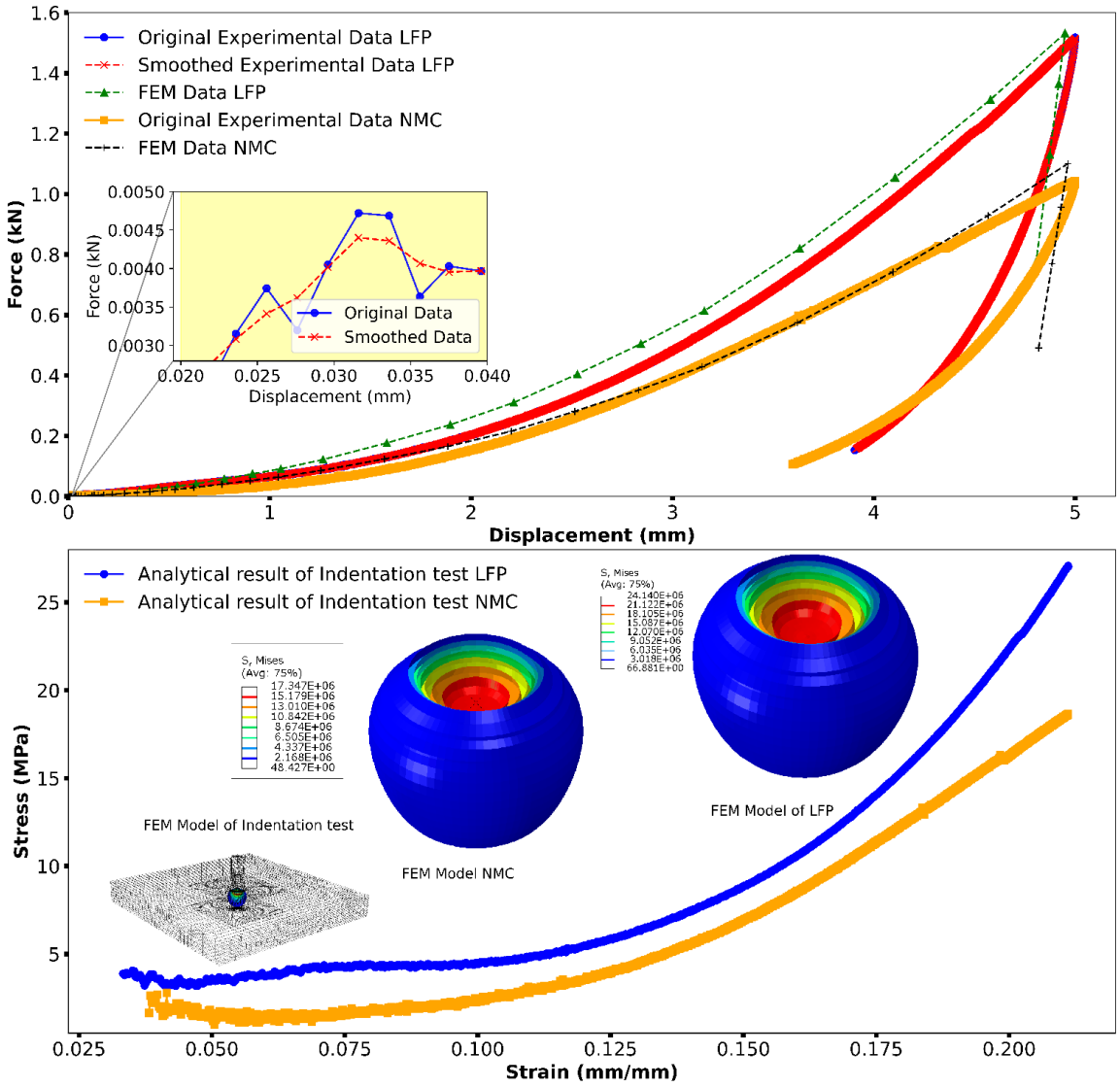

Figure 6. Indentation stress–strain curves obtained during loading and unloading for LFP and NMC cells.

Moreover, by incorporating strain rate analysis and considering the effects of both strain and strain rate from the indentation tests, the developed analytical model can be extended to predict the behaviors of LIB cells in high-impact penetration tests. This is particularly relevant as the same size and geometry projectile used in the indentation tests facilitates a seamless transition to high-impact scenarios. The model's versatility in capturing the dynamic response of LIB cells under varying loading conditions positions it as a valuable tool for predicting performance in scenarios beyond traditional indentation testing:

$$\dot{\varepsilon}_{xx} = \dot{\varepsilon}_{yy} = \frac{d\varepsilon_{xx}}{dt} = \frac{\dot{a}_c}{R} \tag{12}$$

$$\dot{\varepsilon}_{zz} = \frac{d\varepsilon_{zz}}{dt} = \frac{\dot{h}_c}{R} \tag{13}$$

3.2. High-Impact Penetration Test

The final segment of this study involves the implementation of penetration impact tests on LFP and NMC cells. In the previous section, indentation tests were conducted at three different strain rates to probe the effect of strain rate on the battery cell. An analytical and Finite Element (FE) model was developed to convert force-displacement data into stress-strain data, enabling the derivation of a constitutive equation that accurately represents the material properties of the battery cell. This constitutive equation, obtained directly from the indentation tests, was used as the initial input data for predicting the material behavior of battery cells under high-speed impact penetration tests. A Finite Element Analysis (FEA) model was created in ABAQUS/EXPLICIT to simulate the ballistic behavior using this constitutive equation. The distinction between FEM models for indentation and penetration tests lies in the boundary conditions for the projectile, with the projectile provided with an initial velocity in the penetration test scenario

The experimental outcomes, presenting the initial speed and battery cell type, are illustrated in Figure 7. The projectile partially penetrates the battery cells at lower speeds, while complete penetration is observed at higher speeds. It is essential to highlight that the occurrence of partial penetration results in internal short circuits, leading to igniting some cells igniting and generating a significant amount of smoke. An exhaust ventilation system addresses safety concerns and mitigates smoke-related issues. This precautionary measure is essential for ensuring a secure testing environment and effectively managing potential risks associated with the experimental procedures.

Figure 7 displays the results in the form of ballistic curves represented by $V_R - V_0$. These curves are subsequently matched to Equation (14) proposed by Recht and Ipson [50]. This equation calculates the residual velocity (V_R) of the projectile, taking into account the initial velocity (V_0) and the ballistic limit velocity (V_{bl}):

$$V_R = \sqrt[\eta]{(V_0^\eta - V_{bl}^\eta)} \tag{14}$$

where η is a fitting curve. The impact and residual velocities were measured, and the Recht–Ipson constants in Equation (14) were determined through a best fit to the experimental outcomes. For NMC cells, the acquired constants were $\eta = 1.76$ and V_{bl} = 59.7 m/s, while for LFP cells, the values were $\eta = 2.08$ and V_{bl} = 54.8 m/s. Notably, the results indicate total penetration occurred at lower speeds for LFP samples than NMC samples. It is important to highlight that beyond 80 m/s, there is no significant difference in the experimental outcomes. However, in the speed range of 50 to 80 m/s, a substantial disparity between NMC and LFP samples is observed, underscoring the influence of battery type and thickness on the ballistic curve within this speed range.

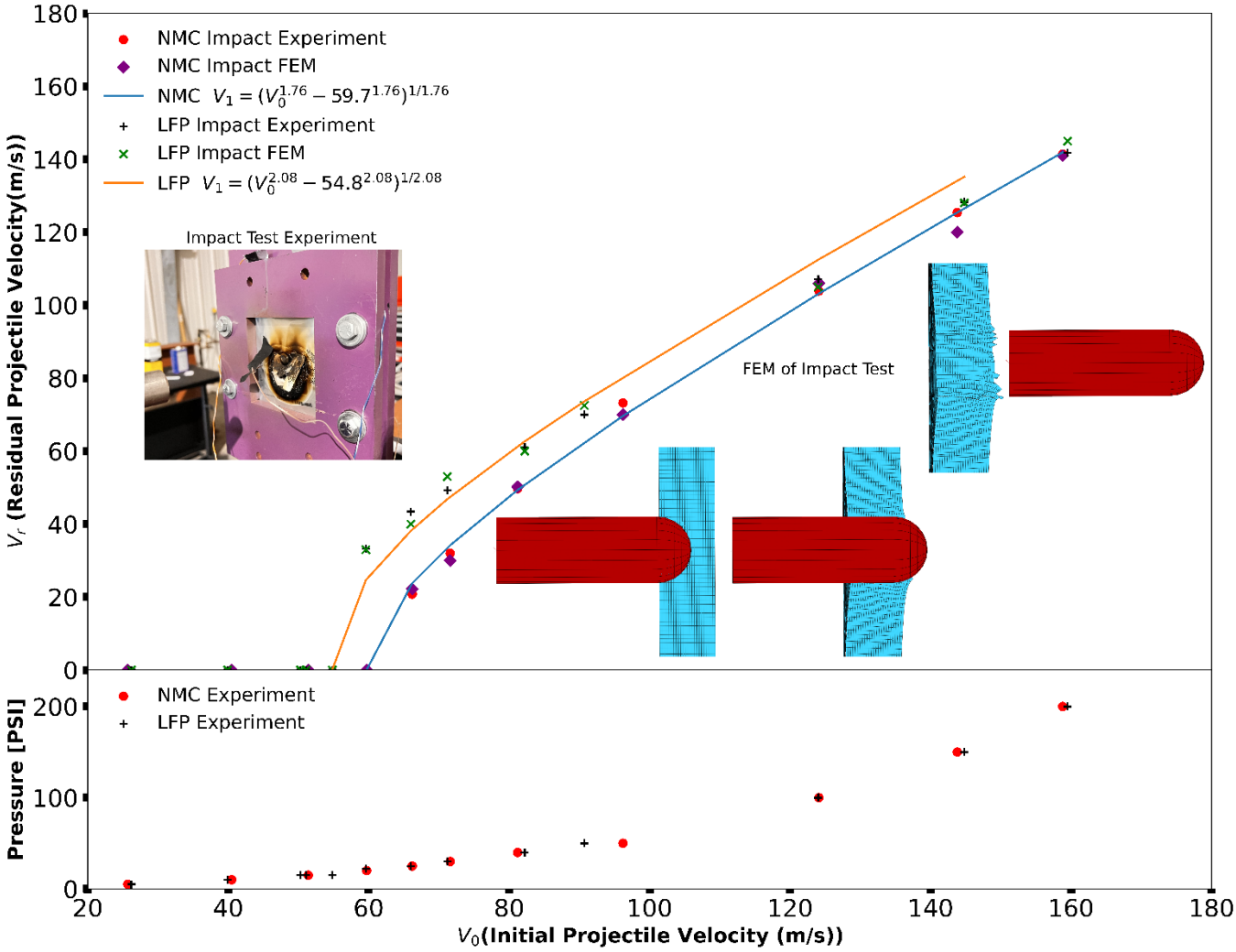

Figure 7. Ballistic curves and characterizing Residual Velocities for NMC and LFP cells impacted at room temperature.

Figure 7 characterizes the residual velocities for NMC and LFP battery cells under high-speed penetration tests, showing the FE model for both LFP and NMC samples. The results show good agreement between experiment and simulation models. However, due to the use of a gas gun for the impact test, Figure 7 includes data for the pressure versus initial velocity, illustrating the relationship between the applied pressure and the resultant velocity. It is clear that based on the geometry and weight of the projectile, the initial velocity created from the pressure will vary.

Furthermore, Figure 7 shows the construction of the ballistic limit curve, where pressures and initial velocities for both LFP and NMC cells were held constant, facilitating a direct comparison with the experimental data. The plotted ballistic limit curve exhibits excellent agreement with the experimental results, indicating a low level of scatter in the test outcomes. This observation underscores the effectiveness of the ballistic limit curve in capturing the ballistic behavior of both LFP and NMC cells under the specified test conditions.

A thermomechanical model was created in Abaqus/Explicit to predict failure initiation in Lithium-ion battery (LIB) cells based on stress, strain rate, and temperature. The same LIB cell and indentation parameters were applied in both static and dynamic loading scenarios. Thus, for this simulation, the same model was utilized, with the addition of a damage model and initial velocity to replicate the indentation test. Unknown parameters for the damage model were identified using a reverse technique. A revised iteration of the original formulation is utilized to pinpoint the initiation of damage within an element. As damage accrues over time, the element experiences a gradual reduction in stiffness until it reaches the maximum damage threshold, ultimately leading to a complete loss of stiffness. The present study opts for the Johnson-Cook model, chosen for its versatility in accommodating temperature and strain rate effects. It is essential to highlight that, given the high plastic strain rate of the LIB cell, adiabatic heating effects have been integrated into this model, indicating the absence of heat conduction between elements.

The expression that outlines the initiation of damage according to the Johnson-Cook model [51] is presented:

$$\overset{\sim}{\varepsilon}{}^{pl}_{\phi} = [d_1 + d_2 exp(-d_3\eta)]\left[1 + d_4 ln\left(\frac{\dot{\varepsilon}^{pl}}{\dot{\varepsilon}_0}\right)\right](1 + d_5\hat{\theta}) \quad (15)$$

In the initial segment of the equation's bracket set, the determination of a fundamental plastic strain value for the initiation of damage relies on a constant denoted as d_1. It is coupled with an exponential function of stress triaxiality represented by η, featuring associated parameters denoted as d_2 and d_3. The subsequent part of the expression introduces strain rate sensitivity through the parameter d_4. This incorporates the natural logarithm of the current equivalent plastic strain rate, denoted as $\dot{\varepsilon}^{pl}$, divided by the strain rate used during the calibration of parameters $d_1 - d_3$, and $\dot{\varepsilon}_0$, the reference strain rate. Lastly, d_5 introduces temperature dependency in the remaining portion of the expression, and the temperature term utilizes the same definition for $\hat{\theta}$ as the plasticity model.

$$\hat{\theta} = \frac{\theta - \theta_t}{\theta_m - \theta_t} \quad (16)$$

where θ represents the current temperature, θ_m is the melting temperature and θ_t is the transition temperature.

This study applies an adiabatic stress analysis where mechanical deformation leads to heating. However, the rapid nature of the high-impact penetration test prevents the generated heat from diffusing through the Lithium-ion battery (LIB) cell promptly. Within the adiabatic analysis, plastic straining results in a heat flux per unit volume, expressed by the following equation:

$$r^{pl} = \beta\sigma : \dot{\varepsilon}^{pl} \quad (17)$$

where r^{pl} signifies the heat flux contributing to the thermal energy balance, β is the user-specified constant for inelastic heat fraction (further elaborated below), and σ represents the stress. The solved heat equation at each integration point is given by:

$$\rho C_p(\theta)\dot{\theta} = r^{pl} \quad (18)$$

Here, ρ stands for the LIB cell's density, C_p denotes specific heat, and the equation expresses the rate of temperature change over time. All material parameters for LFP and NMC cells were reported in Table 4.

Table 4. Material Model Parameters for LIB cells.

Parameters	LFP	NMC
d_1	0.34	0.8
d_2	−0.0126	−0.002
d_3	1.2	1.4
d_4	0	0.6
d_5	0.085	0.1
$\theta_t(^{\circ}C)$	700	700
$\theta_t(^{\circ}C)$	150	150
β	0.9	0.9
$C_p(\theta)\left(\frac{J}{kg^{\circ}C}\right)$	850	850
friction	0.06	0.06

In the evaluation of voltage and temperature changes during indentation tests (static loading) and high penetration tests (dynamic loading), distinct observations emerged, as shown in Figure 8. For the indentation tests on NMC and LFP pouch cells, no discernible alterations were recorded in voltage and temperature, indicating the absence of internal short circuits. Conversely, in high penetration tests where the projectile entirely traversed the battery, both voltage and temperature exhibited no variations, suggesting a lack of connectivity between the collectors and the absence of an ensuing internal short circuit. In contrast, high impact penetration tests involving partial projectile penetration led to a different outcome. Notably, these tests resulted in cell ignition and a decline in voltage, indicative of an internal short circuit occurrence.

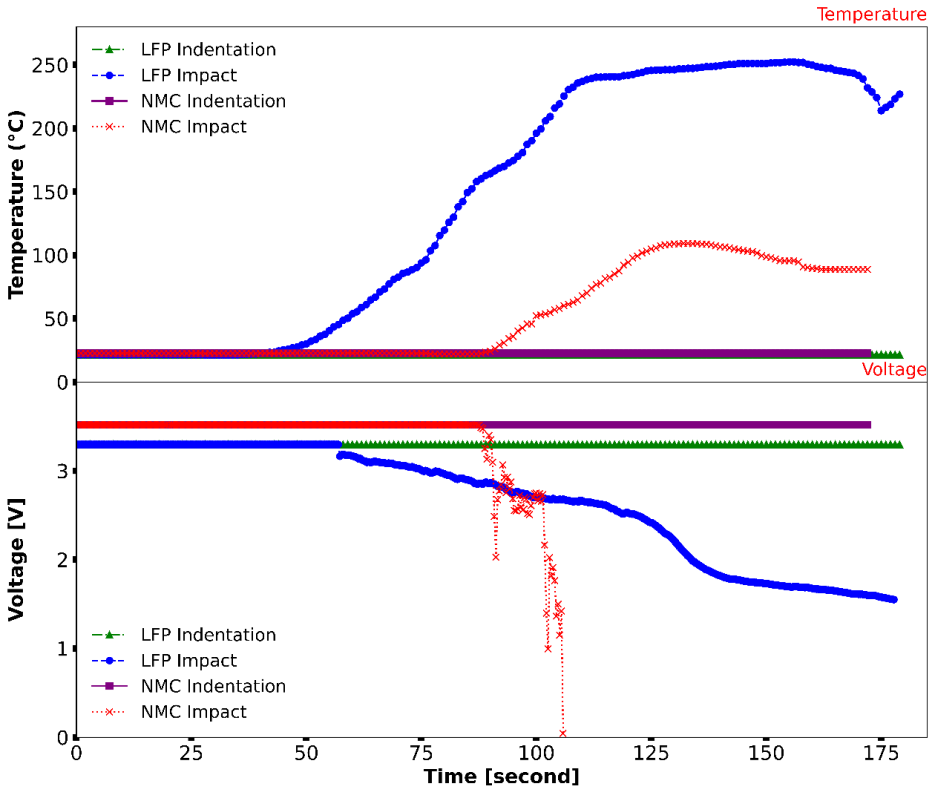

Figure 8. Voltage and temperature response in NMC and LFP pouch cells under indentation and high penetration tests.

Examining high impact penetration tests on lithium-ion batteries revealed a distinctive scenario during partial penetration of the projectile into the battery cells. Despite variations in experimental conditions compared to a nail penetration test, a relevant comparison can be drawn from a study by Chen, M. et al. [52]. This study emphasized the pivotal role of contact resistance between the nail and electrodes in inducing catastrophic failure and heat generation. The observed phenomena in our study align with the findings of Chen et al., underscoring the significance of contact resistance in influencing the outcomes of high impact penetration tests on lithium-ion batteries.

4. Conclusions

This comprehensive study explored the mechanical behavior of Lithium-ion battery (LIB) cells under both quasi-static (Indentation) and dynamic (high-velocity penetration impact) tests, focusing on Lithium Nickel Manganese Cobalt Oxide (NMC) and Lithium Iron Phosphate (LFP) cell types.

This study resolves a significant disparity from earlier studies. In mechanical testing such as indentation tests, pouch battery cells may bulge after a specific penetration depth since their thickness is less than that of other battery cell types, such as cylindrical or prismatic cells. The effect of the bottom platen must be taken into account, as the results cannot accurately depict the pouch cell itself. In order to create a distance between the battery cell and the platen, this study proposed an inhouse fixture. The significant force decrease that is seen while moving from a single cell to a stack of two cells is investigated in this work.

Finding a suitable constitutive equation to express stress–strain data and predict the material behavior of the pouch cells during the impact test is the primary goal of this research. In contrast to previous research that employed tensile or compression testing alone, this study employed an indentation test by using a hemispherical indenter. This study aims to provide an answer to the topic of how stress–strain curves can be generated from an indentation test, given the complexity of geometry in the test. The results demonstrate a strong agreement between the FE and analytical models for converting force–displacement data into stress–strain data. The indenter with the same geometry is used for both quasi-static (indentation) and dynamic (impact) testing to ensure the development of a reliable framework for simulating dynamic situations. This consistent approach provides a robust link between low-speed and high-speed scenarios, enhancing the accuracy of the simulation results. Using a hemispherical indenter in both tests ensures continuity and allows for direct comparison of force–displacement data, leading to more reliable predictions for impact tests.

The finite element method analysis involved the development of a viscoplastic model predicting the indentation test and a thermomechanical model predicting high-speed-impact penetration. A thermomechanical model incorporating stress, strain rate, and temperature could predict failure initiation in LIB cells. The model successfully identified damage initiation based on stress, strain rate, and temperature parameters.

In summary, this research significantly contributes to understanding LIB cell behavior under various loading conditions, providing valuable insights into stress-strain characterization for pouch cells. The findings enhance safety considerations and advance predictive models for the mechanical behavior of LIB cells in high-impact scenarios, contributing to the broader field of electric vehicle safety.

Author Contributions: Writing—reviewing and editing, visualization, simulation, experiment, analytical, E.A.; writing—review and editing, G.Z.V. All authors have read and agreed to the published version of the manuscript.

Funding: This research received no external funding.

Data Availability Statement: The data presented in this study are available on request from the corresponding author. The data are not publicly available due to long-time experiment and rich information.

Acknowledgments: We want to acknowledge that no specific grant numbers were received for this study.

Conflicts of Interest: The authors declare no conflicts of interest.

References

1. Fras, T.; Pawlowski, P.; Li, W.; Wierzbicki, T. Performance of Li-ion pouch batteryunder a high-velocity impact: Experiment and numerical simulation. *Int. J. Impact Eng.* **2021**, *155*, 103915. [CrossRef]
2. Jia, B.; Rusinek, A.; Bahi, S.; Bernier, R.; Pesci, R.; Bendarma, A. Perforation Behavior of 304 Stainless Steel Plates at Various Temperatures. *J. Dyn. Behav. Mater.* **2019**, *5*, 416–431. [CrossRef]
3. Antoinat, L.; Kubler, R.; Barou, J.-L.; Viot, P.; Barrallier, L. Perforation of aluminium alloy thin plates. *Int. J. Impact Eng.* **2015**, *75*, 255–267. [CrossRef]
4. Kisters, T.; Sahraei, E.; Wierzbicki, T. Dynamic impact tests on lithium-ion cells. *Int. J. Impact Eng.* **2017**, *108*, 205–216. [CrossRef]
5. Rodríguez-Millán, M.; Vaz-Romero, A.; Rusinek, A.; Rodríguez-Martínez, J.A.; Arias, A. Experimental Study on the Perforation Process of 5754-H111 and 6082-T6 Aluminium Plates Subjected to Normal Impact by Conical, Hemispherical and Blunt Projectiles. *Exp. Mech.* **2014**, *54*, 729–742. [CrossRef]
6. Numata, D.; Ohtani, K.; Anyoji, M.; Takayama, K.; Togami, K.; Sun, M. HVI tests on CFRP laminates at low temperature. *Int. J. Impact Eng.* **2008**, *35*, 1695–1701. [CrossRef]
7. Chen, Y.; Santhanagopalan, S.; Babu, V.; Ding, Y. Dynamic mechanical behavior of lithium-ion pouch cells subjected to high-velocity impact. *Compos. Struct.* **2019**, *218*, 50–59. [CrossRef]
8. Motaman, S.A.H.; Prahl, U. Microstructural constitutive model for polycrystal viscoplasticity in cold and warm regimes based on continuum dislocation dynamics. *J. Mech. Phys. Solids* **2019**, *122*, 205–243. [CrossRef]
9. Sahraei, E.; Hill, R.; Wierzbicki, T. Calibration and finite element simulation of pouch lithium-ion batteries for mechanical integrity. *J. Power Sources* **2012**, *201*, 307–321. [CrossRef]
10. Wang, H.; Simunovic, S.; Maleki, H.; Howard, J.N.; Hallmark, J.A. Internal configuration of prismatic lithium-ion cells at the onset of mechanically induced short circuit. *J. Power Sources* **2016**, *306*, 424–430. [CrossRef]
11. Jia, Y.; Liu, B.; Hong, Z.; Yin, S.; Finegan, D.P.; Xu, J. Safety issues of defective lithium-ion batteries: Identification and risk evaluation. *J. Mater. Chem. A* **2020**, *8*, 12472–12484. [CrossRef]
12. Lin, H.-C.; Chen, K.-C.; Chen, C.-H. Electrochemical Change Induced by Spherical Indentation in Lithium-Ion Batteries. *Batteries* **2022**, *8*, 268. [CrossRef]
13. Pan, Z.; Li, W.; Xia, Y. Experiments and 3D detailed modeling for a pouch battery cell under impact loading. *J. Energy Storage* **2020**, *27*, 101016. [CrossRef]
14. Tancogne-Dejean, T.; Mohr, D. Indentation of small format Lithium-ion pouch cells: Experiments and modeling. *Int. J. Solids Struct.* **2022**, *257*, 111900. [CrossRef]
15. Xia, Y.; Chen, G.; Zhou, Q.; Shi, X.; Shi, F. Failure behaviours of 100% SOC lithium-ion battery modules under different impact loading conditions. *Eng. Fail. Anal.* **2017**, *82*, 149–160. [CrossRef]
16. Tancogne-Dejean, T.; Grolleau, V.; Mohr, D. Strain rate dependent plasticity of lithium-ion pouch cells: Experiments and simulations. *Int. J. Impact Eng.* **2022**, *159*, 104048. [CrossRef]
17. Chung, S.H.; Tancogne-Dejean, T.; Zhu, J.; Luo, H.; Wierzbicki, T. Failure in lithium-ion batteries under transverse indentation loading. *J. Power Sources* **2018**, *389*, 148–159. [CrossRef]
18. Pérès, J.P.; Perton, F.; Audry, C.; Biensan, P.; de Guibert, A.; Blanc, G.; Broussely, M. A new method to study Li-ion cell safety: Laser beam initiated reactions on both charged negative and positive electrodes. *J. Power Sources* **2001**, *97–98*, 702–710. [CrossRef]
19. Logakannan, K.P.; Zhu, F.; Sypeck, D.; Deng, J.; Kim, S. Impact response of prismatic Li-ion battery jellyrolls and cells. *Int. J. Impact Eng.* **2022**, *170*, 104352. [CrossRef]
20. Zhu, X.; Wang, H.; Wang, X.; Gao, Y.; Allu, S.; Cakmak, E.; Wang, Z. Internal short circuit and failure mechanisms of lithium-ion pouch cells under mechanical indentation abuse conditions: An experimental study. *J. Power Sources* **2020**, *455*, 227939. [CrossRef]
21. Voyiadjis, G.Z.; Akbari, E.; Kattan, P.I. Damage model for lithium-ion batteries with experiments and simulations. *J. Energy Storage* **2023**, *57*, 106285. [CrossRef]
22. Sprenger, M.; Kovachev, G.; Dölle, N.; Schauwecker, F.; Sinz, W.; Ellersdorfer, C. Changes in the Mechanical Behavior of Electrically Aged Lithium-Ion Pouch Cells: In-Plane and Out-of-Plane Indentation Loads with Varying Testing Velocity and State of Charge. *Batteries* **2023**, *9*, 67. [CrossRef]
23. Shi, C.; Wang, T.; Liao, X.; Qie, B.; Yang, P.; Chen, M.; Wang, X.; Srinivasan, A.; Cheng, Q.; Ye, Q.; et al. Accordion-like stretchable Li-ion batteries with high energy density. *Energy Storage Mater.* **2019**, *17*, 136–142. [CrossRef]
24. Voyiadjis, G.Z.; Akbari, E. Novel procedure to determine the stress-strain relation of Lithium-ion Batteries through indentation test. *Appl. Energy* **2023**, *347*, 121492. [CrossRef]
25. Voyiadjis, G.Z.; Akbari, E.; Łuczak, B.; Sumelka, W. Towards Determining an Engineering Stress-Strain Curve and Damage of the Cylindrical Lithium-Ion Battery Using the Cylindrical Indentation Test. *Batteries* **2023**, *9*, 233. [CrossRef]
26. Wang, H.; Kumar, A.; Simunovic, S.; Allu, S.; Kalnaus, S.; Turner, J.A.; Helmers, J.C.; Rules, E.T.; Winchester, C.S.; Gorney, P. Progressive mechanical indentation of large-format Li-ion cells. *J. Power Sources* **2017**, *341*, 156–164. [CrossRef]

27. Kermani, G.; Sahraei, E. Dynamic impact response of lithium-ion batteries, constitutive properties and failure model. *RSC Adv.* **2019**, *9*, 2464–2473. [CrossRef]
28. Johnson, G.R.; Cook, W.H. Fracture characteristics of three metals subjected to various strains, strain rates, temperatures and pressures. *Eng. Fract. Mech.* **1985**, *21*, 31–48. [CrossRef]
29. Luo, H.; Xia, Y.; Zhou, Q. Mechanical damage in a lithium-ion pouch cell under indentation loads. *J. Power Sources* **2017**, *357*, 61–70. [CrossRef]
30. Zhang, C.; Xu, J.; Cao, L.; Wu, Z.; Santhanagopalan, S. Constitutive behavior and progressive mechanical failure of electrodes in lithium-ion batteries. *J. Power Sources* **2017**, *357*, 126–137. [CrossRef]
31. Duan, X.; Li, J.; Jia, Y.; Gao, X.; Wang, L.; Xu, J. Understanding of Stress-Driven Internal Short Circuit Mechanisms in Lithium-Ion Batteries with High SOCs. *Adv. Sci.* **2023**, *2023*, 2302496. [CrossRef]
32. Wang, H.; Duan, X.; Liu, B. The anisotropic homogenized model for pouch type lithium-ion battery under various abuse loadings. *J. Electrochem. Energy Convers. Storage* **2021**, *18*, 021015. [CrossRef]
33. Liu, Y.; Mao, Y.; Wang, H.; Pan, Y.; Liu, B. Internal short circuit of lithium metal batteries under mechanical abuse. *Int. J. Mech. Sci.* **2023**, *245*, 108130. [CrossRef]
34. Keshavarzi, M.M.; Gilaki, M.; Sahraei, E. Characterization of in-situ material properties of pouch lithium-ion batteries in tension from three-point bending tests. *Int. J. Mech. Sci.* **2022**, *219*, 107090. [CrossRef]
35. Jia, Y.; Gao, X.; Ma, L.; Xu, J. Comprehensive Battery Safety Risk Evaluation: Aged Cells versus Fresh Cells Upon Mechanical Abusive Loadings. *Adv. Energy Mater.* **2023**, *13*, 2300368. [CrossRef]
36. Duan, X.; Wang, H.; Jia, Y.; Wang, L.; Liu, B.; Xu, J. A multiphysics understanding of internal short circuit mechanisms in lithium-ion batteries upon mechanical stress abuse. *Energy Storage Mater.* **2022**, *45*, 667–679. [CrossRef]
37. Abaqus, G. *Abaqus 6.11*; Dassault Systemes Simulia Corporation: Providence, RI, USA, 2011; p. 3.
38. Jankowiak, T.; Rusinek, A.; Kpenyigba, K.; Pesci, R. Ballistic behavior of steel sheet subjected to impact and perforation. *Steel Compos. Struct.* **2014**, *16*, 595–609. [CrossRef]
39. Clyne, T.W.; Campbell, J.E.; Burley, M.; Dean, J. Profilometry-Based Inverse Finite Element Method Indentation Plastometry. *Adv. Eng. Mater.* **2021**, *23*, 2100437. [CrossRef]
40. Teague, E.C.; Scire, F.E.; Baker, S.M.; Jensen, S.W. Three-dimensional stylus profilometry. *Wear* **1982**, *83*, 1–12. [CrossRef]
41. Shimizu, Y.; Chen, L.-C.; Kim, D.W.; Chen, X.; Li, X.; Matsukuma, H. An insight into optical metrology in manufacturing. *Meas. Sci. Technol.* **2021**, *32*, 042003. [CrossRef]
42. Field, J.S.; Swain, M.V. A simple predictive model for spherical indentation. *J. Mater. Res.* **1993**, *8*, 297–306. [CrossRef]
43. Taljat, B.; Zacharia, T.; Kosel, F. New analytical procedure to determine stress-strain curve from spherical indentation data. *Int. J. Solids Struct.* **1998**, *35*, 4411–4426. [CrossRef]
44. Xu, B.; Chen, X. Determining engineering stress-strain curve directly from the load-depth curve of spherical indentation test. *J. Mater. Res.* **2010**, *25*, 2297–2307. [CrossRef]
45. Mesarovic, S.D.; Fleck, N.A. Spherical indentation of elastic–plastic solids. *Proc. R. Soc. Lond. Ser. A Math. Phys. Eng. Sci.* **1999**, *455*, 2707–2728. [CrossRef]
46. Qu, S.; Huang, Y.; Pharr, G.; Hwang, K. The indentation size effect in the spherical indentation of iridium: A study via the conventional theory of mechanism-based strain gradient plasticity. *Int. J. Plast.* **2006**, *22*, 1265–1286. [CrossRef]
47. Feng, G.; Qu, S.; Huang, Y.; Nix, W. An analytical expression for the stress field around an elastoplastic indentation/contact. *Acta Mater.* **2007**, *55*, 2929–2938. [CrossRef]
48. Johnson, K.L.; Johnson, K.L. *Contact Mechanics*; Cambridge University Press: Cambridge, UK, 1987.
49. Oliver, W.C.; Pharr, G.M. An improved technique for determining hardness and elastic modulus using load and displacement sensing indentation experiments. *J. Mater. Res.* **1992**, *7*, 1564–1583. [CrossRef]
50. Recht, R.F.; Ipson, T.W. Ballistic Perforation Dynamics. *J. Appl. Mech.* **1963**, *30*, 384–390. [CrossRef]
51. O'Donoghue, W. *Bayesian Model Calibration of a Mechanical Finite Element Model of an LR61 Alkaline Battery*; The University of Alabama in Huntsville: Huntsville, AL, USA, 2023.
52. Chen, M.; Ye, Q.; Shi, C.; Cheng, Q.; Qie, B.; Liao, X.; Zhai, H.; He, Y.; Yang, Y. New Insights into Nail Penetration of Li-Ion Batteries: Effects of Heterogeneous Contact Resistance. *Batter. Supercaps* **2019**, *2*, 874–881. [CrossRef]